SAND2011-7040C

Bridging the Gap between Complex Numerical Modeling and Rapid Scenario Assessment: A Dimensionless Parameter Approach for Enhanced Geothermal Systems

Elena Kalinina, Teklu Hadgu, Sean A. McKenna, Thomas Lowry

Sandia National Laboratories, MS 1369, P.O. Box 5800, Albuquerque, NM 87185

Sandia National Laboratories is a multi-program laboratory managed and operated by Sandia Corporation, a wholly owned subsidiary of Lockheed Martin Corporation, for the U.S. Department of Energy's National Nuclear Security Administration under contract DE-AC04-94AL85000.

Keywords

Geothermal, reservoir simulation, EGS, system dynamics, heat transport, dimensionless temperature drawdown

Abstract

Assessing the timing, cost, and market competitiveness of geothermal energy production requires understanding the thermal performance of the reservoir, but numerical models of reservoir performance can be complex and time consuming to execute. The computational overhead and numerical complexity runs counter to the needs of real-time scenario analysis and the propagation of uncertainties in the physical, technological, and economical parameters. The ability of existing analytical solutions to simulate realistic heat transfer in a reservoir is limited by the complexity of the system.

Here, we develop an approach for utilizing output from complex numerical models in a rapidly deployable systems based assessment model. The approach generates a series of dimensionless temperature drawdown curves based on the numerical modeling of a number of reservoir conditions that are specific to enhanced geothermal systems (EGS). This approach allows for substituting a complicated numerical solution with lookup tables that can be used in system dynamic assessment models.

We considered a homogeneous 3-dimensional reservoir. A series of simulations were run by varying the distance between the injection and production wells, the permeability, the reservoir thickness, the mass injection rate, the injection temperature, the initial reservoir temperature, the porosity and the reservoir depth. These simulations were done using FEHM (finite element multi-phase flow and heat and mass transport computer code, Los Alamos National Laboratories) to compute the temperature drawdown $T(t)$ in the production well. The $T(t)$ curves were converted into dimensionless $T_d(t_d)$ curves. Dimensionless temperature (T_d) and time (t_d) were defined similarly to the corresponding dimensionless parameters in Gringarten et al. solution. The approach was verified by using the dimensionless curves to predict temperature drawdown and comparing the predicted curves with the FEHM simulations.

Introduction

Geothermal energy development requires analysis of a number of complex systems to evaluate accessibility of a resource, existing technologies, power demands, economics, and other important conditions. To perform such analysis, a full suite of the systems and sub-systems needs to be considered. A system dynamics model is being developed by Sandia National Laboratories (Lowry et. al, 2010) to address this need. This model represents an integrated systems modeling tool that allows a user to perform scenario assessments for different geothermal applications.

The model simulates heat and fluid flow through the entire EGS process. The current version of the model calculates heat exchange between the reservoir and fluid using one of two analytical solutions; the Carslaw and Jaeger (Carslaw and Jaeger, 1959) solution for a single fracture, and the Gringarten (Gringarten et al., 1975) solution for a series of infinite parallel fractures. The analytical solutions rely on a number of simplifications and are limited in their capabilities to represent the actual reservoir conditions. One example of the analytical solution limitation is provided in Appendix A. The system dynamics model would significantly benefit from incorporating more realistic reservoir simulations if these simulations would not interfere with its capability to provide near real-time scenario analysis.

One of the possible approaches to this problem is being developed through a series of numerical heat transport simulations using 3-D finite element heat and mass transport computer code FEHM (Zyvoloski, et al., 1997). This approach allows for substituting complicated numerical solutions with lookup tables (or response surfaces) that can be used in system dynamic assessment models.

Objective

The major objective of this work was to develop an approach for incorporating realistic reservoir simulations into the system dynamics model. The output from a numerical reservoir simulation that is required as an input into the system dynamics model is the temperature drawdown as a function of time in each of the producing wells during the operational period of the power plant. These temperature drawdowns need to be calculated for a specified set of uncertain parameters being considered by a scenario. These parameters include injection rate, well separation distance, injection temperature, reservoir temperature, depth of geothermal resource, reservoir thickness, and reservoir permeability.

It was assumed that the temperature drawdowns calculated by the numerical reservoir model for a number of representative reservoir conditions can be converted to dimensionless curves (or type curves) that can be used to generate temperature versus time for any given set of parameters. The purpose of this work was to demonstrate whether this assumption is credible for homogeneous reservoir conditions. The approach was verified (or tested) by using the dimensionless curves to predict temperature drawdown.

It is assumed that a similar approach can be developed to incorporate heterogeneous reservoir conditions and that development will be addressed in future work.

Methods

The reservoir simulations were performed using a numerical model domain shown in Figure 1. The model simulates heat transport in the porous medium and is implemented with the computer code FEHM (Zyvoloski, et al., 1997). The grid block dimensions in the *x* and *y* direction are 5 m by 5 m. The grid block dimension in the *z* direction is 37.5 m. The fine grid in *x* and *y* direction was required to generate heterogeneous permeability and porosity fields using the fractured continuum model approach (McKenna and Reeves, 2005) for heterogeneous reservoir simulations. The fine discretization also allows for a more accurate representation of heat and fluid flow around the boreholes.

The homogeneous reservoir conditions were considered first with the effective permeability and porosity specified within the enhanced permeability volume defined based on the reservoir thickness and well separation distance. The permeability outside of this volume was set equal to $10^{-17}m^2$.

The modeling domain shown in Figure 1 represents one quarter of a 5-point injection scheme (1 injector & 4 producers). The location of the injection well remains the same (front, left corner of the cube) in all the simulations. The production well is placed at the different distances along the cube diagonal. The separation distance of 800 m was used in the base case simulation.

The pre-injection boundary conditions are hydrostatic pressures and constant temperature on the vertical sides of the cube, constant pressure and temperature on the top, and zero flux on the bottom. The injection boundary conditions are zero flux across all the boundaries. Injection is implemented using a fixed injection rate, which is equally sub-divided between the vertical grid nodes representing the injection well. The injection interval corresponds to the reservoir thickness. The production well is implemented by specifying fixed drawdown pressures in the production well nodes.

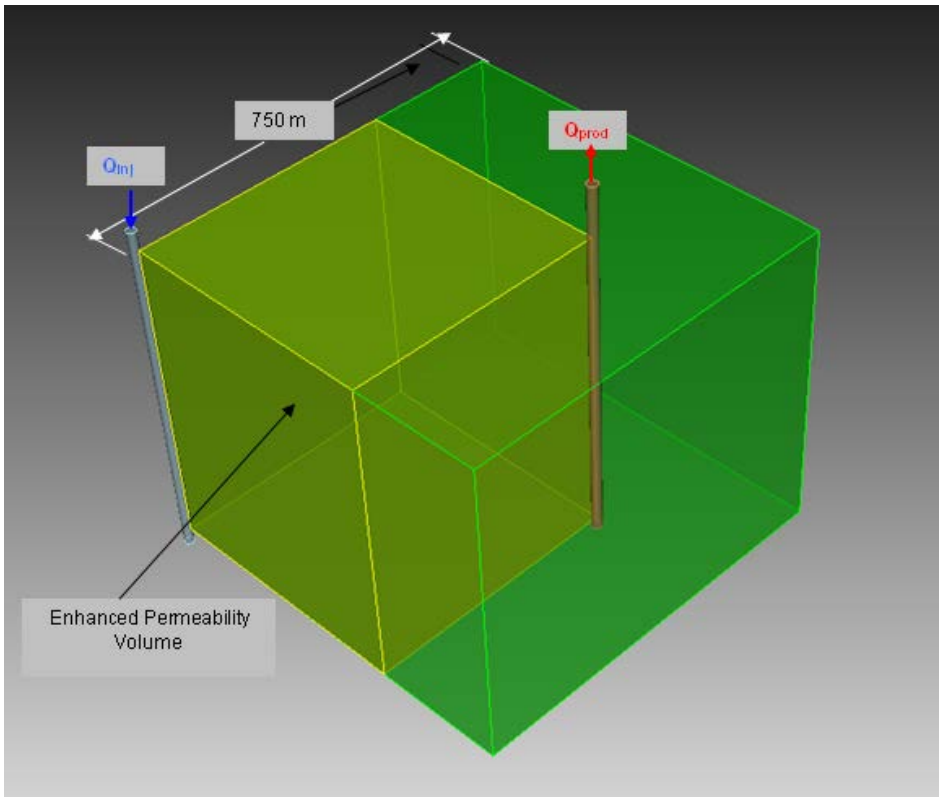

Figure 1. Conceptual Representation of the Reservoir Numerical Model

The following rock properties were used in all the simulations to be consistent with the systems dynamic model (Lowry, et al., 2010): rock bulk density of 2,600 kg/m^3; rock specific heat capacity of 9.5x10^{-4} MJ/kg-K; and rock heat conductivity of 3.0 W/m-K.

The following parameters were varied in the different simulations:

- Effective permeability [m^2]: 1x10^{-13}; 5x10^{-13}; 1x10^{-12}; 5x10^{-12}; 1x10^{-11}.
- Effective porosity [-]: 0.004, 0.01, 0.04.
- Depth to the reservoir top boundary [m]: 4,000; 5,000; and 6,000
- Reservoir thickness [m]: 450; 600; 750
- Reservoir temperature [^{0}C]: 175, 225, 250.
- Well separation distance [m]: 800 and 1,000.
- Injection temperature [^{0}C]: 20, 50, and 80
- Injection rate [kg/s]: 30; 60; and 90.

Note that the total injection rate shown above is 4 times the injection rate used in the model.

The base case considered reservoir thickness of 750 m, well separation distance of 800 m, injection rate of 30 kg/s, reservoir temperature of 225^{0}C, injection temperature of 80^{0}C, depth to the model top of 4,000 m, effective porosity of 0.01, and effective permeability of 5x10^{-13} m^2. Each simulation following the base case considered change in one parameter compared to the base case.

The range of the parameters used in the simulations was dictated by the corresponding ranges implemented in the system dynamics model, except for the effective permeability and porosity values. The analytical solutions currently implemented in the system dynamics model are for fracture flow and they use fracture parameters instead of porous medium continuum parameters defined in the numerical simulations.

Temperature versus time at the bottom of the production well were obtained for each numerical simulation. The results of these simulations are presented in Figures 2 through 8 using dimensionless temperature versus dimensionless time format. The actual temperature versus the actual time are shown for two cases (Figure 10 and Figure 11) to demonstrate the thermal front retardation relative to the fluid front under the different conditions.

The dimensionless temperature (T_d) and time (t_d) were defined as follows, which are similar to the definitions in Gringarten et al. (1975):

$$t_d = \frac{(\rho_w c_w)^2}{\rho_r c_r K_r}\left[\frac{Q}{LBN_{fr}}\right]^2 (t - t_{lag}) \quad (1)$$

$$T_d = \frac{T_{res} - T}{T_{res} - T_{inj}} \quad (2)$$

Here t is the actual time; ρ_w is the water density; c_w is the water specific heat capacity; ρ_r is the rock density; c_r is the rock specific heat capacity; K_r is the rock thermal conductivity; Q is the injection rate; L is the well separation distance; B is the reservoir thickness; N_{fr} is the number of fractures (an arbitrary parameter in the case of porous medium); and t_{lag} is the thermal front travel time between the injection and production wells.

Note that the term $\frac{(\rho_w c_w)^2}{\rho_r c_r K_r}$ changes very little (from 2.03×10^6 to 2.07×10^6 s/m^2) within the reservoir temperature range considered. The parameter N_{fr} was set equal to 3.5 to obtain the dimensionless time scale similar to the one in Gringarten et al. (1975).

The examples in Figures 2 through 7 show the dimensionless thermal drawdowns for the different injection temperatures, reservoir temperatures, depths to the reservoir top, well separation distances, reservoir thicknesses, and effective porosities. As it can be seen from these figures, when the actual temperatures are converted to the dimensionless temperatures the resulting curves follow each other very closely and are nearly identical across Figures 2 through 7. A linear adjustment was needed for the reservoir thicknesses of 450 m and 600 m. In these two cases the denominator LxBx N_{fr} in Equation (1) was multiplied by a coefficient to get the match shown in Figure 6.

Figure 8 shows dimensionless drawdowns for a range of the effective permeability values that can be expected in an enhanced reservoir. There is one “type” curve per each effective permeability value similar to one type curve per each dimensionless fracture spacing (x_{ed}) in Gringarten et al. (1975). The Gringarten’s type curves are reproduced in Figure 8 from Gringarten et al., (1975, Figure 3) to allow for a qualitative comparison.

The dimensionless fracture spacing (x_{ed}) is defined in Gringarten (1975) as:

$$x_{ed} = \frac{\rho_w c_w}{K_r}\left[\frac{Q}{LBN_{fr}}\right]x_e \qquad (3)$$

where x_e is half fracture spacing.

The dimensionless curve corresponding to the effective permeability of $5x10^{-13}$ m^2 shown in Figure 8 is close to the Gringarten's curve for x_{ed} =7. The fracture spacing (2 x_e) corresponding to x_{ed} =7 and to the parameters Q, L, B, and N_{fr} used in this simulation can be calculated from Equation (3). The fracture aperture (b) can be calculated from Snow's equation (Snow, 1968):

$$k = \frac{b^3}{24 x_e} \qquad (4)$$

where k is effective permeability.

The resulting fracture spacing and fracture aperture are 40 m and 0.25 mm respectively. Both parameters seem to be reasonable from the physical point of view.

The numerical type curves enclose a smaller area than analytical type curves. This is probably due to the fact that the reservoir dimensions are constrained in the numerical situation and the analytical solution domain is infinite.

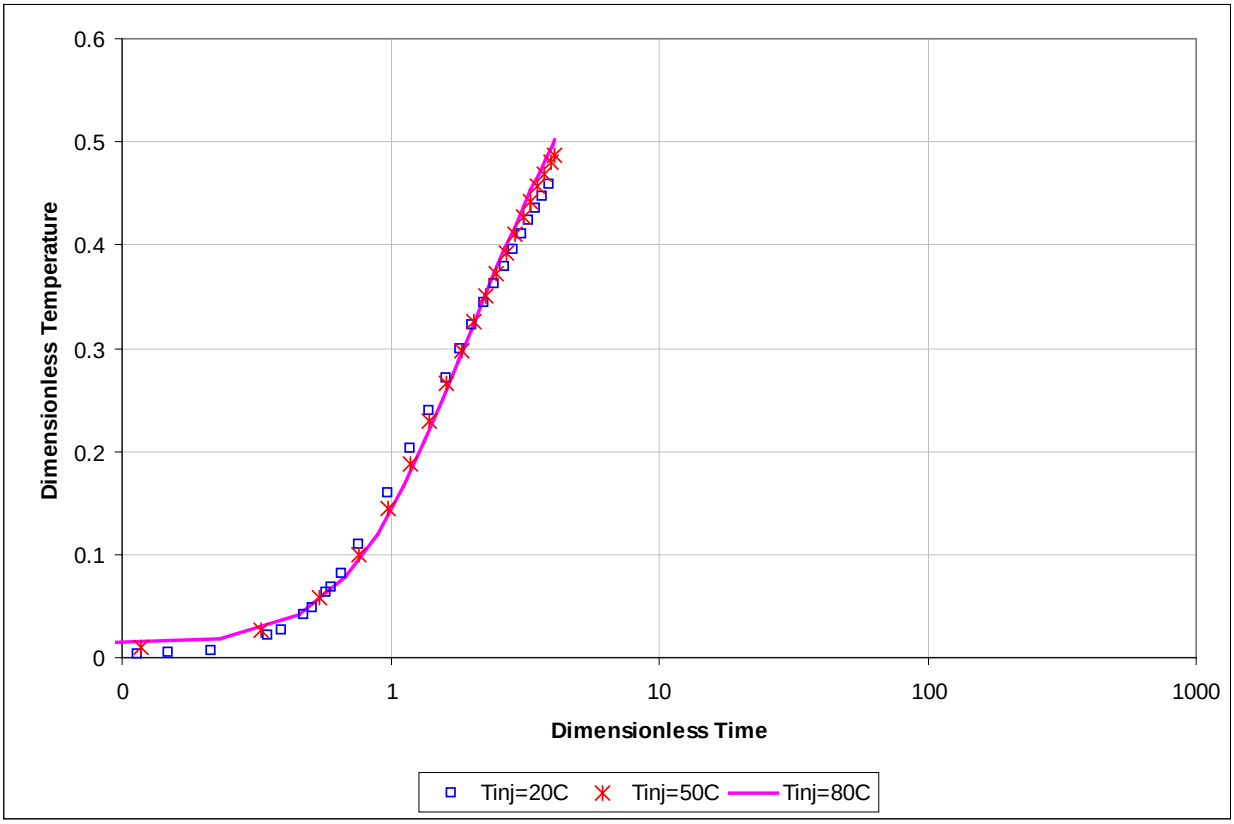

NOTE: Base case injection temperature is 80^0C

Figure 2. Dimensionless Temperature Drawdowns for the Simulations with the Different Injection Temperatures

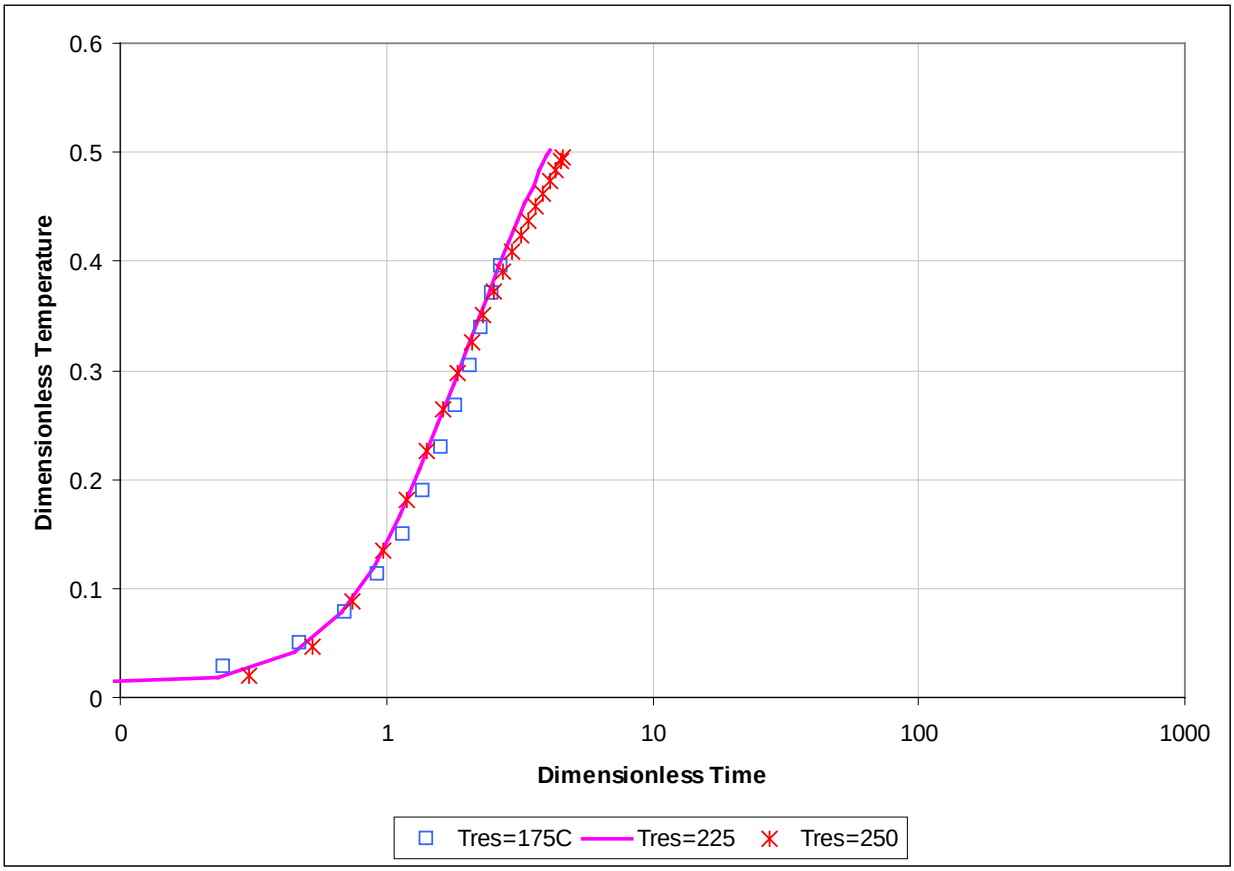

NOTE: Base case reservoir temperature is 225^0C

Figure 3. Dimensionless Temperature Drawdowns for the Simulations with the Different Reservoir Temperatures

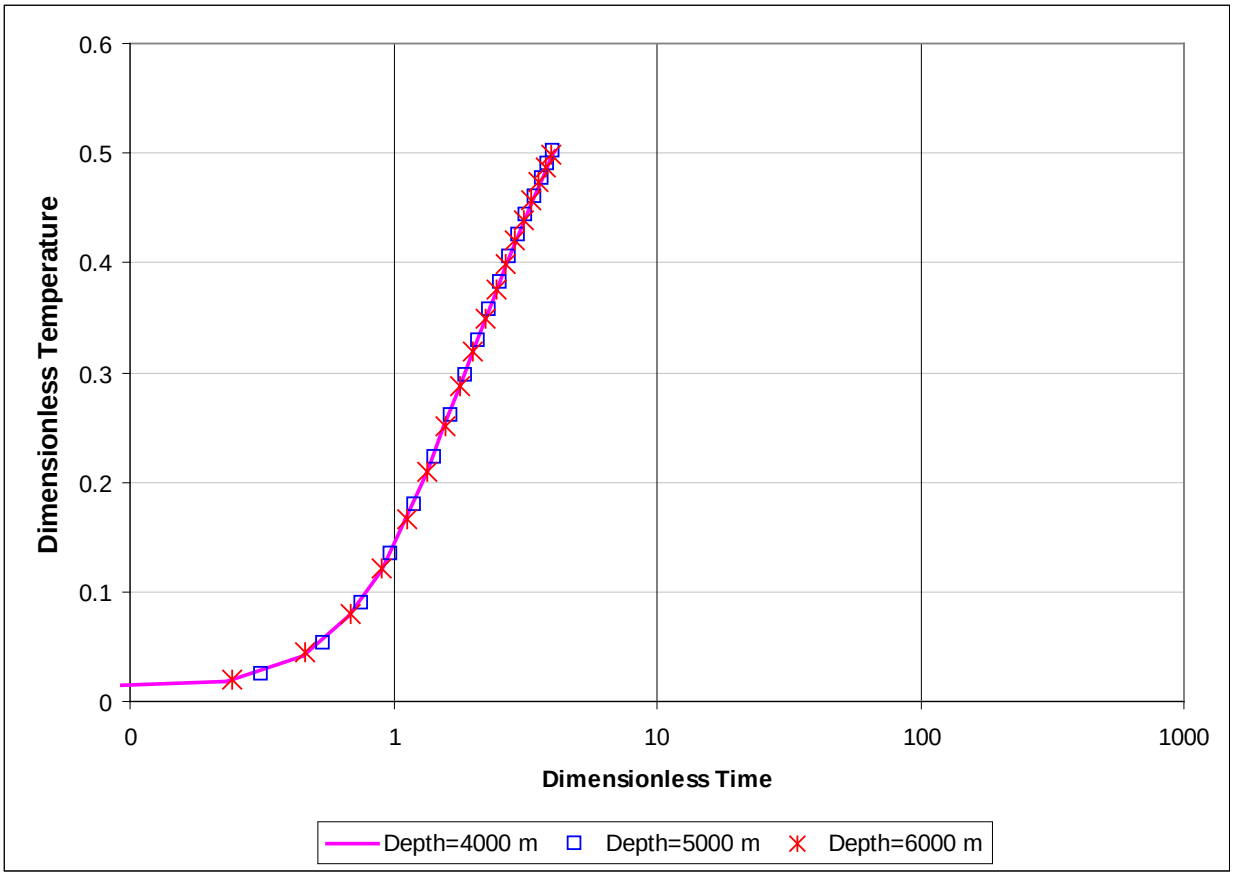

NOTE: Base case depth to the reservoir top is 4,000 m

Figure 4. Dimensionless Temperature Drawdowns for the Simulations with the Different Depths to the Reservoir Top

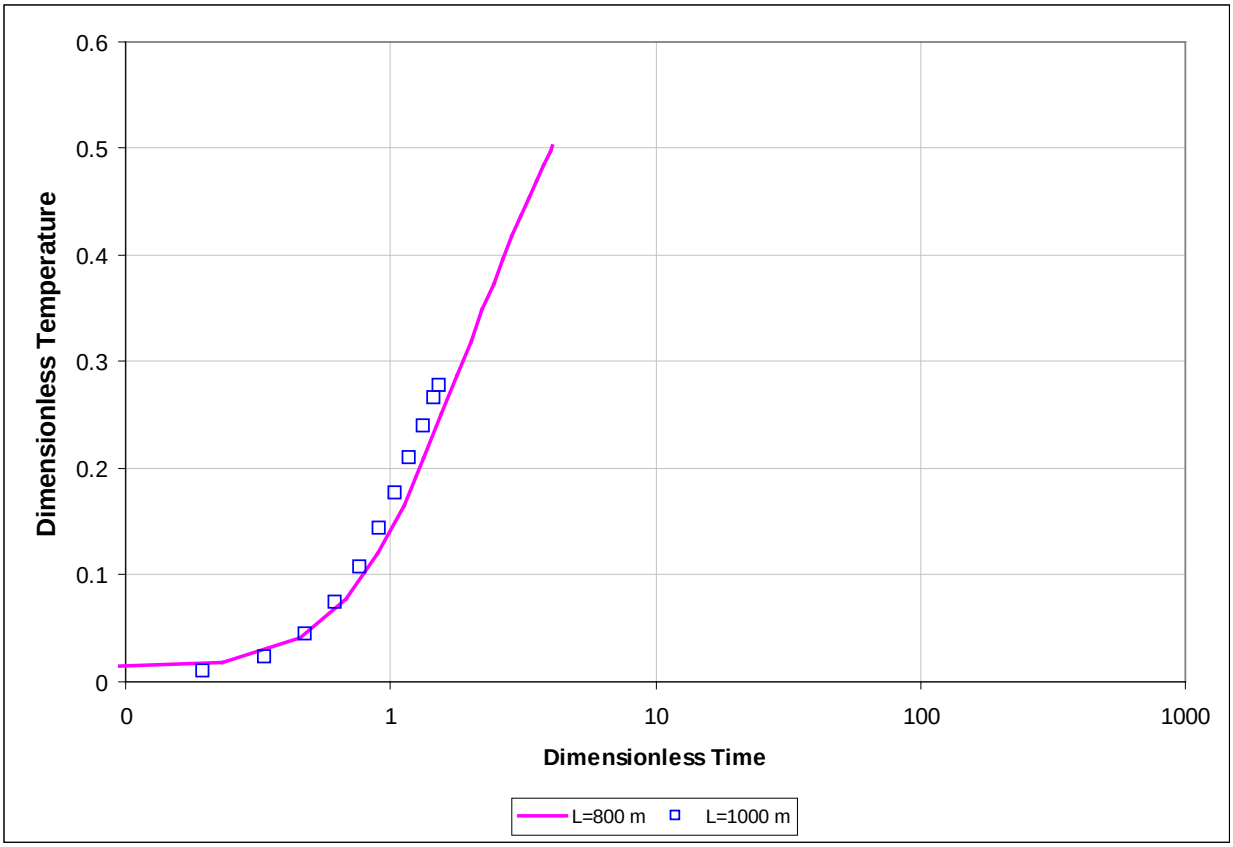

NOTE: Base case well separation distance (L) is 800 m

Figure 5. Dimensionless Temperature Drawdowns for the Simulations with the Different Well Separation Distances.

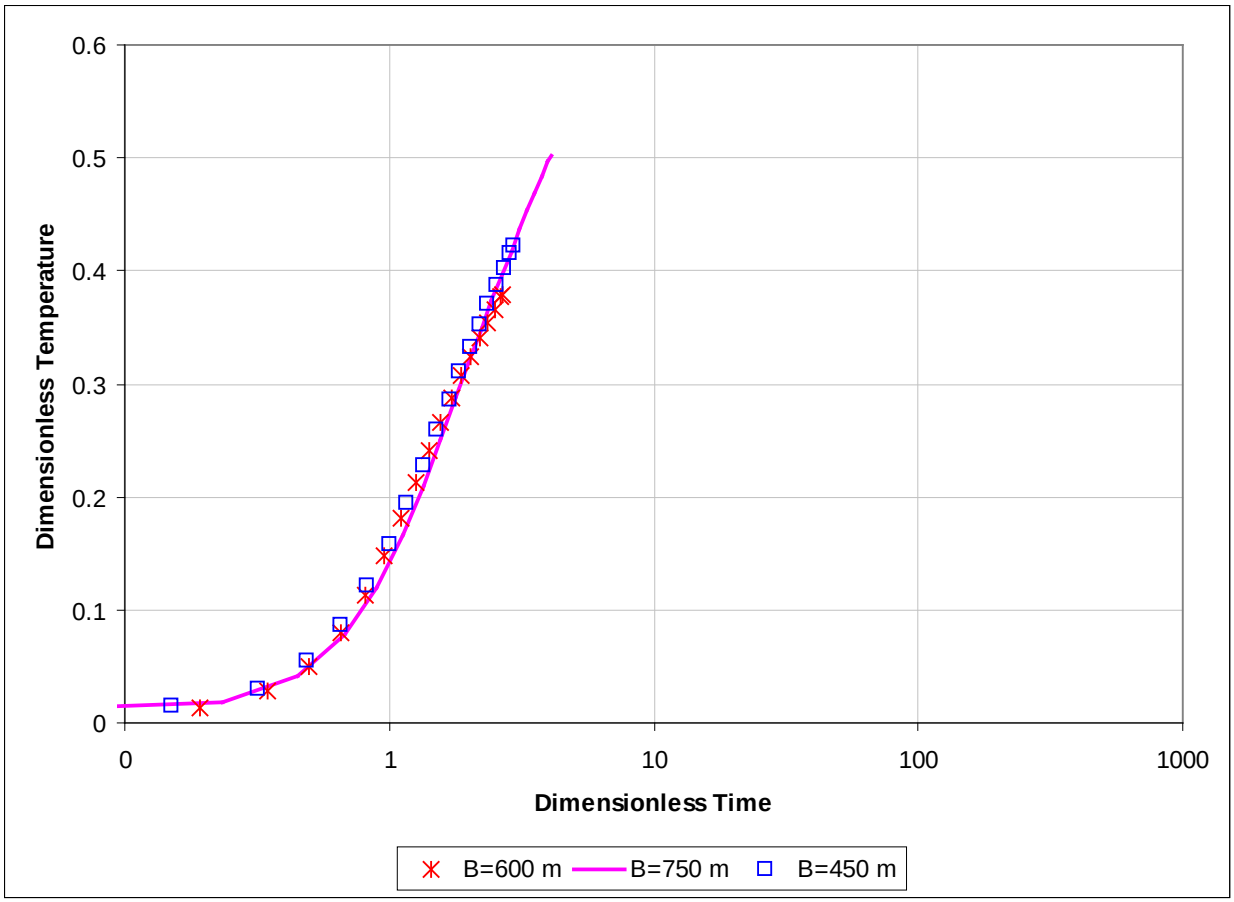

NOTE: Base case reservoir thickness (*B*) is 750 m

Figure 6. Dimensionless Temperature Drawdowns for the Simulations with the Different Reservoir Thicknesses.

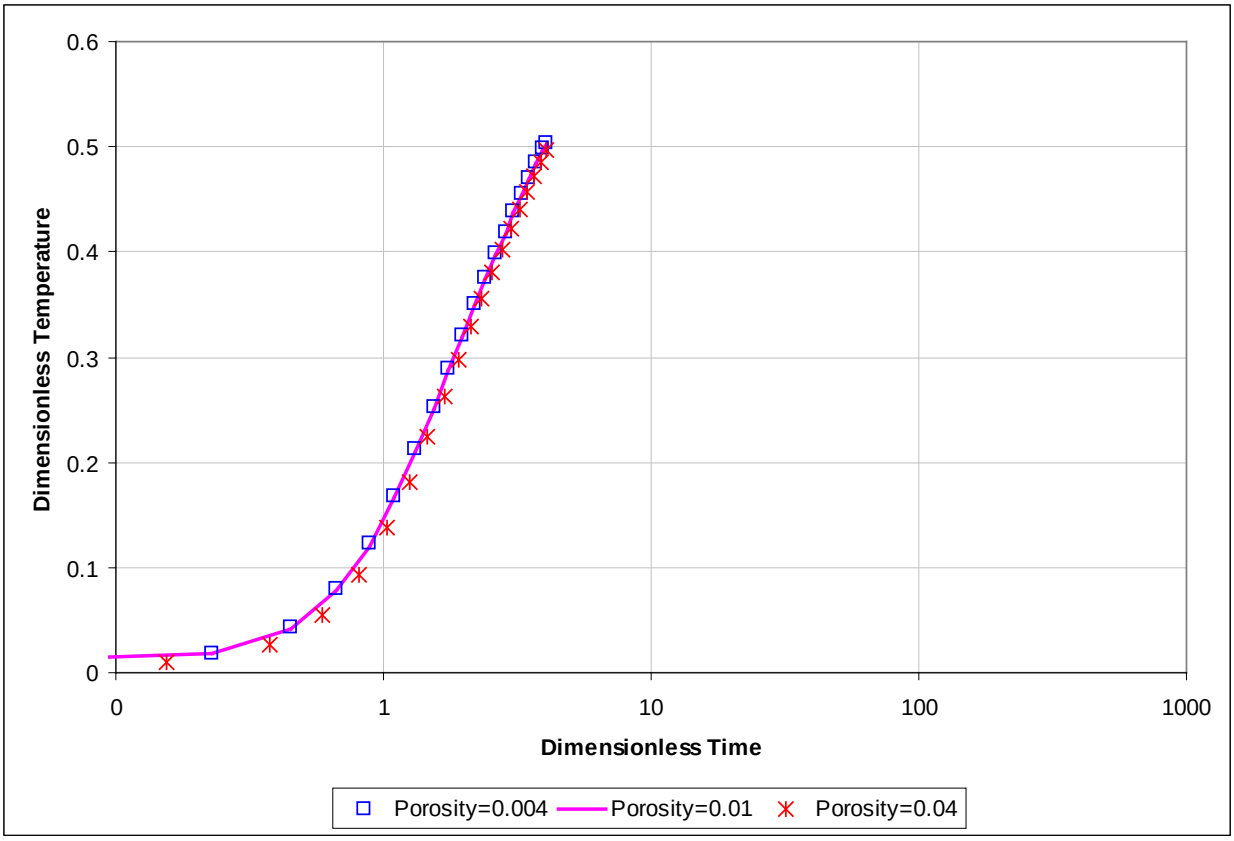

NOTE: Base case reservoir effective porosity is 0.01

Figure 7. Dimensionless Temperature Drawdowns for the Simulations with the Different Reservoir Effective Porosities.

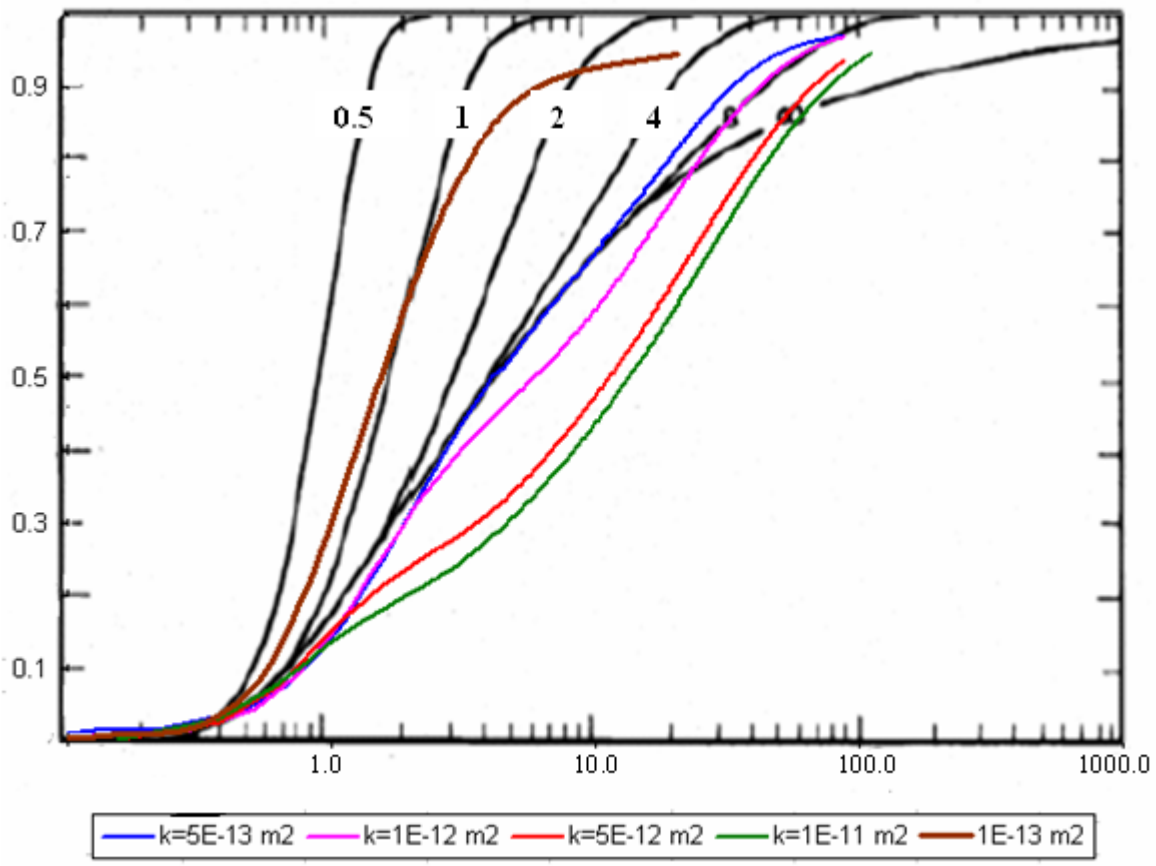

NOTE: Base case reservoir permeability (k) is 5×10^{-13} m^2

Figure 8. Dimensionless Temperature Drawdowns for the Simulations with the Different Effective Permeabilities.

The dimensionless curve approach was verified by using the dimensionless curves to predict temperature drawdowns, and by comparing these predicted drawdowns to the calculated ones. The following parameters were used in this test case: reservoir thickness (B) of 600 m, reservoir temperature (T_{res}) of 200^{0}C, injection temperature (T_{inj}) of 60^{0}C, depth to the reservoir top (D) of 5,000 m, effective permeability (k) of 1×10^{-11} m^2, effective porosity (ε) of 0.01, well separation distance (L) of 800 m, and injection rate (Q) of 45 kg/s. These parameters were not evaluated in any previous simulations.

Figure 9 shows the temperature versus time obtained from the numerical simulation (calculated drawdowns) and temperature versus time calculated from the dimensionless curve corresponding to the effective permeability of 1×10^{-11} m^2 (predicted drawdowns). A good match was obtained between calculated and predicted temperatures during the 30 year operational period.

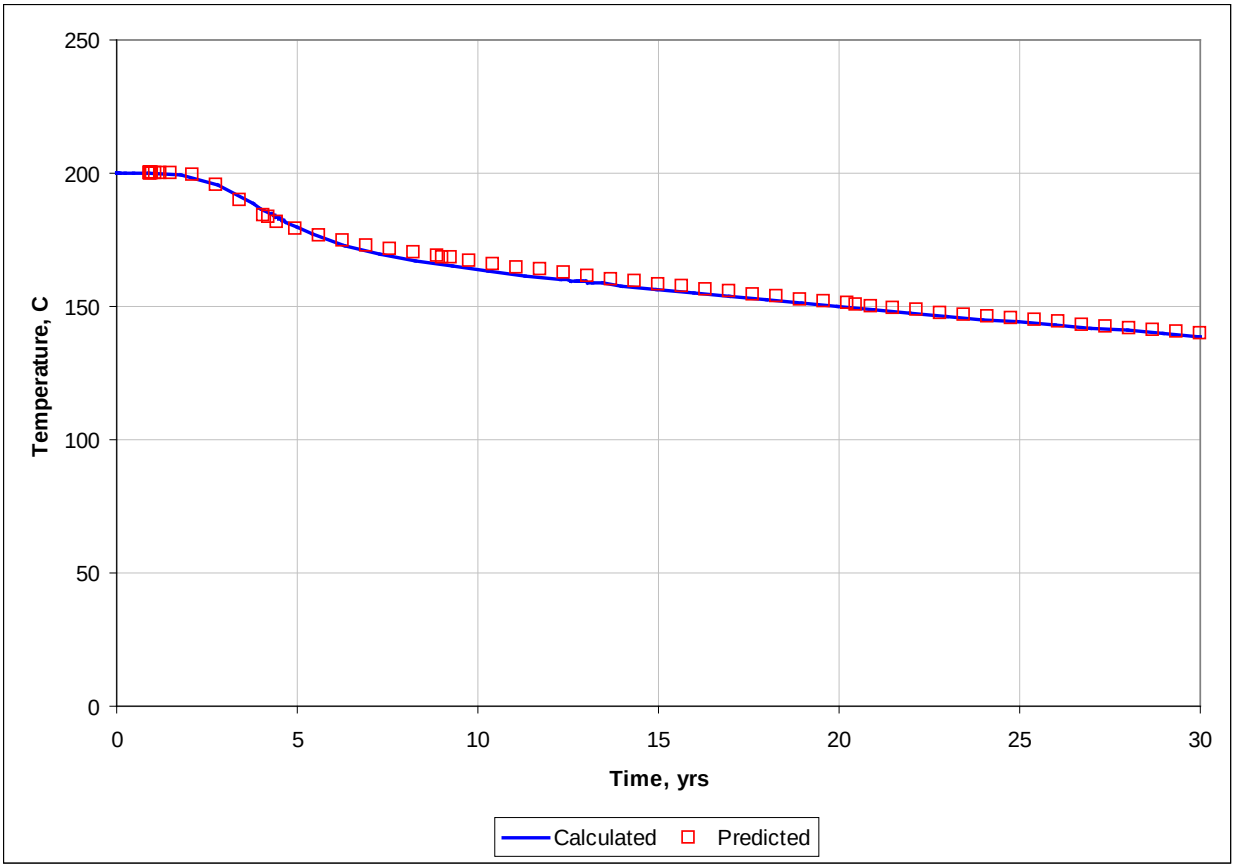

NOTE: The following parameters were used in this test: B=600 m, T_{res}=200^{0}C, T_{inj}=60^{0}C, D=5,000 m, k=1x10^{-11} m^2, ε=0.01, L= 800 m, Q=45 kg/s.

Figure 9. Calculated and Predicted Temperature Drawdowns

To use the dimensionless curve approach described above, one needs to know the thermal front travel time between the injection and production wells (t_{lag}). This is the time when the first noticeable change in temperature occurs at the production well (the temperature drawdown is equal to or greater than 0.1% of T_{res}). Starting form this time, the temperature at the production well sharply decreases for some period of time, which is followed by a slower decrease later in time. Two different cases are discussed below. The first case demonstrates conditions in which the travel times are very different. The second case demonstrates conditions in which the travel times are practically the same.

The temperatures versus time are shown in Figure 10 for three simulations with the different reservoir temperatures. All the other parameters used in these simulations were the same. As it can be seen from this figure, the thermal breakthrough times, the time at which the temperatures first drop from the reservoir temperature, are very different – 6,600 days for T_{res} =175^{0}C; 4,200 days for T_{res} =225^{0}C; and 3,400 days for T_{res} =250^{0}C. As it can be seen from these data, the thermal breakthrough time is almost 2 times longer when reservoir temperature is 175^{0}C compared to reservoir temperature of 250^{0}C. The thermal breakthrough time is 1.24 times longer when reservoir temperature is 175^{0}C compared to reservoir temperature of 225^{0}C.

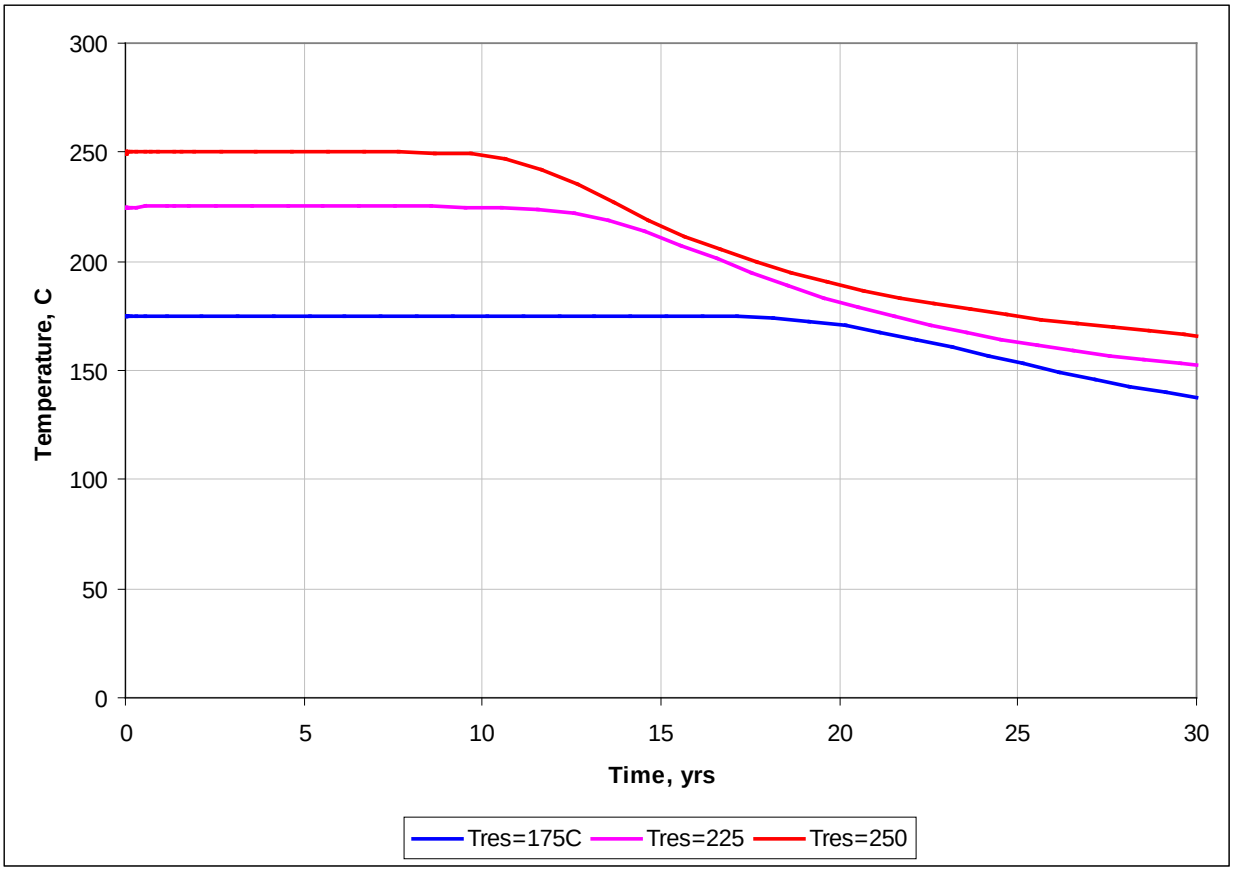

NOTE: All parameters are the same as in the base case, except the reservoir temperatures used in 2 simulations.

Figure 10. Temperature Drawdowns in the Production Well for Different Reservoir Temperatures

The temperatures versus time are shown in Figure 11 for three simulations with the different effective porosities. All the other parameters used in these simulations were the same. . As it can be seen from this figure, the effective porosity within the range considered (0.004 to 0.04) has insignificant impact on the thermal breakthrough time and on the thermal drawdowns in the production well.

These results can be explained by estimating velocity of the thermal front and corresponding thermal breakthrough times under the different reservoir temperatures and porosities taking into account temperature dependent density and viscosity of water.

The thermal front velocity was estimated as:

$$u_T = \frac{u}{R} \tag{5}$$

$$u = \frac{v_l}{\varepsilon} \tag{6}$$

where v_l is Darcy's velocity, ε is effective porosity, and R is thermal retardation factor.

The Darcy's velocity v_l is calculated in FEHM as (Equation 8 in Zyvoloski, et al., 1997):

$$v_l = \frac{k}{\mu_l}\overline{\nabla} P_l - \frac{kg}{\eta_l} \qquad (7)$$

The thermal retardation factor R is defined as:

$$R = 1 + \frac{(1-\varepsilon)\rho_r c_r}{\varepsilon \rho_l c_l} \qquad (8)$$

where ρ_l is the water density; ρ_l is the water specific heat capacity; ρ_r is the rock density; and c_r is the rock specific heat capacity. Note that Equation 8 was derived based on assumptions such single phase flow, thermodynamic equilibrium between the rock and the fluid, incompressible rock, constant thermal properties of both the rock and the fluid, and neglecting thermal conduction.

According to this estimation, the thermal front velocity is about 2 times higher (the thermal breakthrough time is 2 times faster) in the reservoir with the initial temperature of 250^0C than in the reservoir with the initial temperature of 175^0C and 1.3 times faster than in the reservoir with the initial temperature of 225^0C. This conclusion is consistent with the numerical simulation results shown in Figure 10.

Note that the thermal retardation factor is almost the same for all three cases (around 64) because the product of ρ_l and c_l does not change significantly with temperature (density decreases and specific heat increases). However, the thermal front velocity increases with temperature due to increase in seepage velocity. Also note that the thermal breakthrough time is significantly longer than the water breakthrough time.

In the simulations with the different effective porosities the thermal breakthrough times are similar because lower porosity leads to increasing both, seepage velocity and retardation factor, as well as higher porosity leads to decreases in both of these parameter values. As a result, the ratio of seepage velocity and retardation factor only slightly changes from one reservoir porosity case to another.

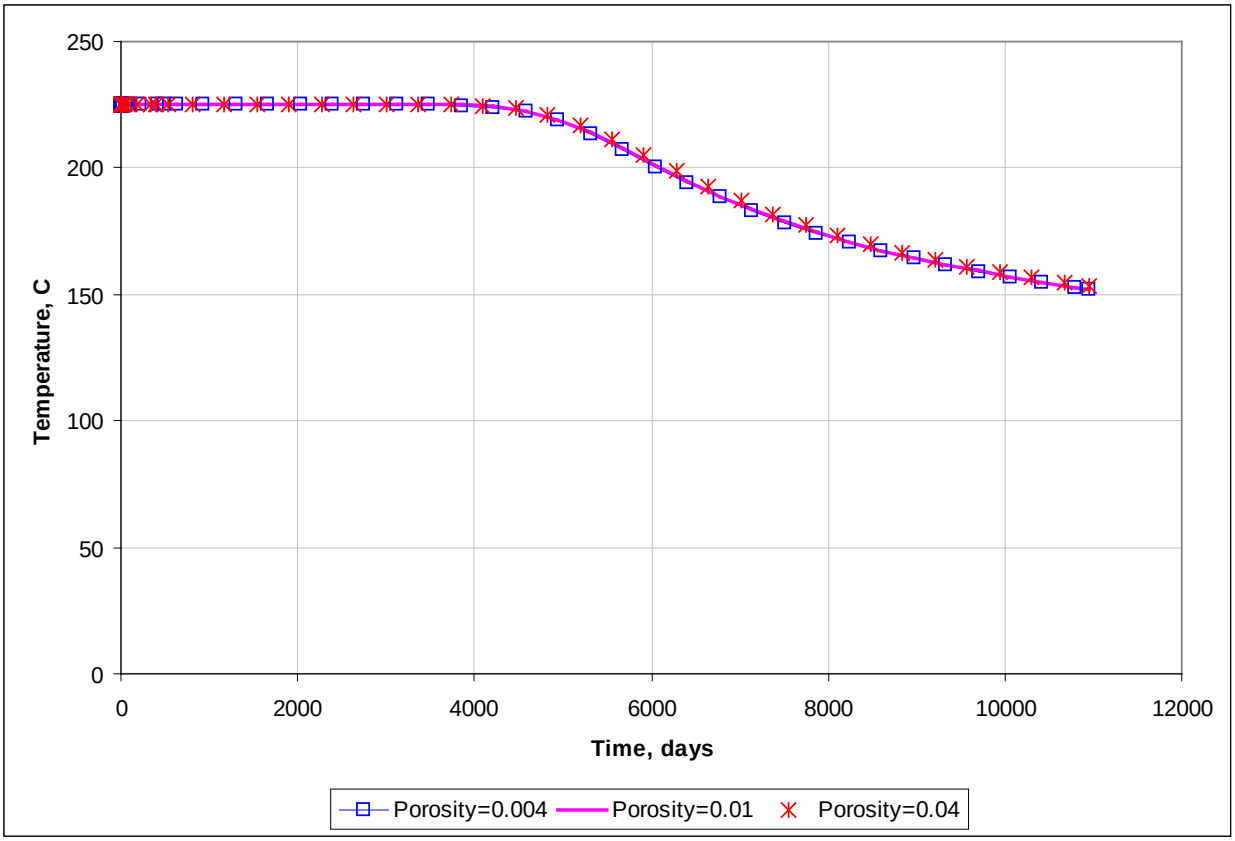

NOTE: All parameters are the same as in the base case, except the effective porosities used in 2 simulations.

Figure 11. Temperature Drawdowns in the Production Well for Different Effective Porosities

Summary

The current work considered an approach that allows for converting multiple numerical reservoir simulations into the dimensionless type curves. Each curve represents a dimensionless temperature response of a homogeneous reservoir with a fixed effective permeability. This dimensionless curve can be converted into the actual temperature drawdowns during the operational period using the reservoir specific parameters and injection characteristics such as the reservoir thickness, reservoir temperature, well separation distance, injection temperature, and injection rate. It was shown that the reservoir porosity and the depth of the reservoir have insignificant effects on the temperature drawdowns in the production well. The dimensionless curves were generated for a 5-point injection scheme and thus are limited to this specific configuration.

The approach was verified by using the dimensionless curves to predict temperature drawdown. The predicted drawdowns were then compared with the calculated drawdowns obtained from the corresponding numerical simulation.

Work is underway to consider the effects of heterogeneous reservoir permeability and porosity on the temperature drawdowns. The applicability of the dimensionless curve approach will be tested for the heterogeneous reservoir conditions. The goal is to account for heterogeneity via lumped parameters that can be incorporated in the dimensionless curve approach.

References

Carslaw, H. S. and J. C. Jaeger, 1959. "Conduction of Heat in Solids." *Oxford, Clarendon Press*.
Gringarten, A. C., P. A. Witherspoon, and Y.Ohnishi, 1975. "Theory of Heat Extraction from Fractured Hot Dry Rock." *Journal of Geophysical Research 80(8)*.
Lowry, T.S., V.C. Tidwell, P.H. Kobos, D.A.Blankenship, 2010. "A Multi-Tiered System Dynamics Approach for Geothermal Systems Analysis and Evaluation." Geothermal Resources Council *Transactions, v. 34, p. 85-90*.
McKenna, S. A. and P. C. Reeves, 2005. "Fractured Continuum Approach to Stochastic Permeability Modeling" in T. C. Coburn, J. M. Yarus, and R. L. Chambers, eds., *"Stochastic Modeling and Geostatistics: Principles, Methods, and Case Studies", v. II, p. 1–14.*
Snow, D. T., 1968. "Rock Fracture Spacings, Openings, and Porosities." *Journal of the Soil Mechanics and Foundations Division, Proceedings of American Society of Civil Engineers, v. 94, p. 73-91*.
Zyvoloski, G.A., B.A. Robinson, Z.V. Dash, and L.L. Trease, 1997. "Summary of the Models and Methods for the FEHM Application - A Finite-Element Heat- and Mass-Transfer Code." *LA-13307-MS, Los Alamos, New Mexico: Los Alamos National Laboratory.*

Appendix A: Example of a Calculation Using Gringarten's Solution

The example demonstrates a situation in which the applicability of the analytical solution for infinite parallel fractures may be limited.

Figure A-1 shows the dimensionless type curves of Gringarten et al., (1975) for the different dimensionless fracture spacing. Let's assume that the required dimensionless temperature at the end of the operational period is 0.6. This requirement can be met with 4 pairs of t_d-x_{ed} values as shown in Figure A-1 and summarized in Table A-1.

Let's assume the following parameters: reservoir thickness of 450 m, reservoir temperature of 200^0C, injection temperature of 60^0C, production rate of 360 kg/s, well separation distance of 700 m.

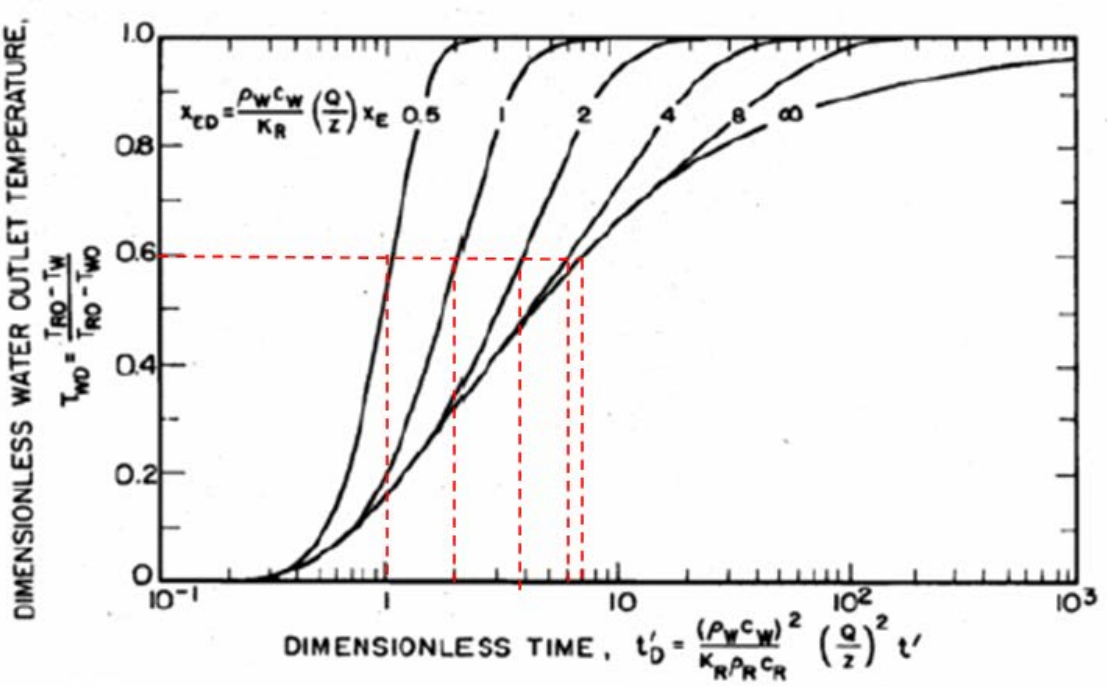

NOTE: This figure was reproduced from Figure 3 in Gringarten (1975). The red dashed lines were added to the original figure to illustrate the example calculation.

Figure A-1. Dimensionless Temperature versus Dimensionless Time for the Different Fracture Spacing

The half fracture spacing x_e can be calculated for each t_d-x_{ed} pair using Equations (1) and (3) and assuming t_{lag} equal to 0. The number of fractures N_{fr} can be calculated from Equation (3). The values of x_e and N_{fr} are provide in Table A-1. Note that $2x_eN_{fr}$ represents the length perpendicular to the fractures ($L^{\perp}$). As it can be seen from Table A-1, in the case of x_{ed} equal to 4 or greater, the length of the system ($L^{\perp}$>2,500 m) may be greater than a size of a typical reservoir.

Table A-1. Calculated Half Fracture Spacing (x_e), Number of Fractures (N_{fr}), and total Length Perpendicular to the Fracture Orientation ($L^{\perp}$)

x_{ed}	t_d	x_e, m	N_{fr}	$L^{\perp}$, m
0.5	1	17	52	1764
1	2	24	37	1762
2	3.9	35	26	1807
4	5.6	58	22	2517
8	7	103	20	4032